Giant pyroelectricity in nanomembranes

https://doi.org/10.1038/s41586-022-04850-7

Received: 17 May 2020

Accepted: 11 May 2022

Published online: 20 July 2022

Check for updates

Jie Jiang[1,8]✉, Lifu Zhang[1,8], Chen Ming[2], Hua Zhou[3], Pritom Bose[4], Yuwei Guo[1], Yang Hu[1], Baiwei Wang[1], Zhizhong Chen[1], Ru Jia[1], Saloni Pendse[1], Yu Xiang[5], Yaobiao Xia[5], Zonghuan Lu[5], Xixing Wen[5], Yao Cai[6], Chengliang Sun[6], Gwo-Ching Wang[5], Toh-Ming Lu[5], Daniel Gall[1], Yi-Yang Sun[2], Nikhil Koratkar[1,4], Edwin Fohtung[1], Yunfeng Shi[1]✉ & Jian Shi[1,7]✉

Pyroelectricity describes the generation of electricity by temporal temperature change in polar materials[1–3]. When free-standing pyroelectric materials approach the 2D crystalline limit, how pyroelectricity behaves remained largely unknown. Here, using three model pyroelectric materials whose bonding characters along the out-of-plane direction vary from van der Waals (In_2Se_3), quasi-van der Waals ($CsBiNb_2O_7$) to ionic/covalent (ZnO), we experimentally show the dimensionality effect on pyroelectricity and the relation between lattice dynamics and pyroelectricity. We find that, for all three materials, when the thickness of free-standing sheets becomes small, their pyroelectric coefficients increase rapidly. We show that the material with chemical bonds along the out-of-plane direction exhibits the greatest dimensionality effect. Experimental observations evidence the possible influence of changed phonon dynamics in crystals with reduced thickness on their pyroelectricity. Our findings should stimulate fundamental study on pyroelectricity in ultra-thin materials and inspire technological development for potential pyroelectric applications in thermal imaging and energy harvesting.

Pyroelectricity is the temperature fluctuation (temporal temperature gradient) response of the spontaneous polarization in pyroelectric materials. It has been widely used in thermal imagings[3], sensors[4], nanogenerators[5], energy harvesters[5,6], hydrogen generation[7] and nuclear fusion[8]. One of the unique advantages of pyroelectric devices is the ultra-fast response down to picoseconds[9]. The understanding of polarization and pyroelectricity based on the classic Clausius–Mossotti model[10] with the assumption of identifiable 'polarization centres' is not precise because the electronic charge in a real crystal has a periodic continuous distribution instead of localized contributions. Later, the development of the modern theory of polarization (Berry phase polarization) considers the electron cloud distribution but focuses on the contribution of static lattice[10]. The pyroelectric coefficient p, measuring the 'ability' of polarization change with fixed temperature fluctuation, is mainly contributed by the primary pyroelectricity p_1 (at constant external strain but vibrating lattice, so-called 'clamped-lattice' pyroelectricity) and the secondary pyroelectricity p_2 (combined effects of piezoelectricity and thermal expansion)[3].

In 1945, Born found a quantum-mechanical solution of the primary pyroelectricity out of harmonic vibrations of ions[1]. Born's theory can be understood by the renormalization of electronic states owing to electron–phonon interactions. The redistribution of the electron cloud (when $dT/dt > 0$) is shown in Fig. 1b with respect to the original state (when $dT/dt = 0$) in Fig. 1a. With the Taylor expansion of the electron–phonon interaction $V(r - l - u_l)$ about the atomic displacements $u_l = 0$ with respect to their average position l (r denotes the position of the electron), the Hamiltonian is[11,12]

$$\mathcal{H} = \mathcal{H}_0 + \mathcal{H}_1 + \mathcal{H}_2 = \mathcal{H}_0 + \sum_l u_l \nabla_l V(r-l) + \frac{1}{2}\sum_l u_l u_l \nabla_l \nabla_l V(r-l), \quad (1)$$

in which $\mathcal{H}_0$ is given by neglecting u_l and $\nabla_l V(r - l)$ is the change in electron-lattice potential per unit displacement of atom. In the harmonic approximation, $\mathcal{H}_1$ is dropped because the thermal averaging of u_l is vanished. $\mathcal{H}_2$ induces a second-order redistribution of the electron cloud, which is known as the Debye–Waller (DW) term. The DW term represents one electron interacting with two phonons once. This electron–phonon renormalization is related to the mean square displacement $\langle u_l^2 \rangle$, contributing to pyroelectricity. For example, in pyroelectrics, the electron clouds could become more delocalized when $dT/dt > 0$ (Fig. 1b) than their original states when $dT/dt = 0$ (Fig. 1a).

Later, in 1975, Szigeti complemented Born's theory by taking an anharmonic-potential term (also known as the internal strain) into account and showed its contribution to the primary pyroelectricity[2]. Thus, the overall primary pyroelectric coefficient is expressed as[2,13]:

$$p_1 = p_1^{(1)} + p_1^{(2)} = \sum_a \frac{\partial P_S}{\partial Q_a}\frac{d\langle Q_a \rangle}{dT} + \sum_j \frac{\partial^2 P_S}{\partial Q_j^2}\frac{d\langle Q_j^2 \rangle}{dT}, \quad (2)$$

in which P_S is the spontaneous polarization, Q_a is the active normal coordinate producing polarization in the direction of P_S, Q_j is the normal coordinate, $p_1^{(1)}$ is the first-order primary pyroelectric coefficient owing to the rigid-ion displacement (the internal-strain term) and $p_1^{(2)}$ is the second-order contribution owing to the electron–phonon

[1]Department of Materials Science and Engineering, Rensselaer Polytechnic Institute, Troy, NY, USA. [2]State Key Laboratory of High Performance Ceramics and Superfine Microstructure, Shanghai Institute of Ceramics, Chinese Academy of Sciences, Shanghai, China. [3]X-ray Science Division, Advanced Photon Source, Argonne National Laboratory, Lemont, IL, USA. [4]Department of Mechanical, Aerospace, and Nuclear Engineering, Rensselaer Polytechnic Institute, Troy, NY, USA. [5]Department of Physics, Applied Physics, and Astronomy, Rensselaer Polytechnic Institute, Troy, NY, USA. [6]The Institute of Technological Sciences, Wuhan University, Wuhan, China. [7]Center for Materials, Devices, and Integrated Systems, Rensselaer Polytechnic Institute, Troy, NY, USA. [8]These authors contributed equally: Jie Jiang, Lifu Zhang. ✉e-mail: jiangj2@rpi.edu; shiy2@rpi.edu; shij4@rpi.edu

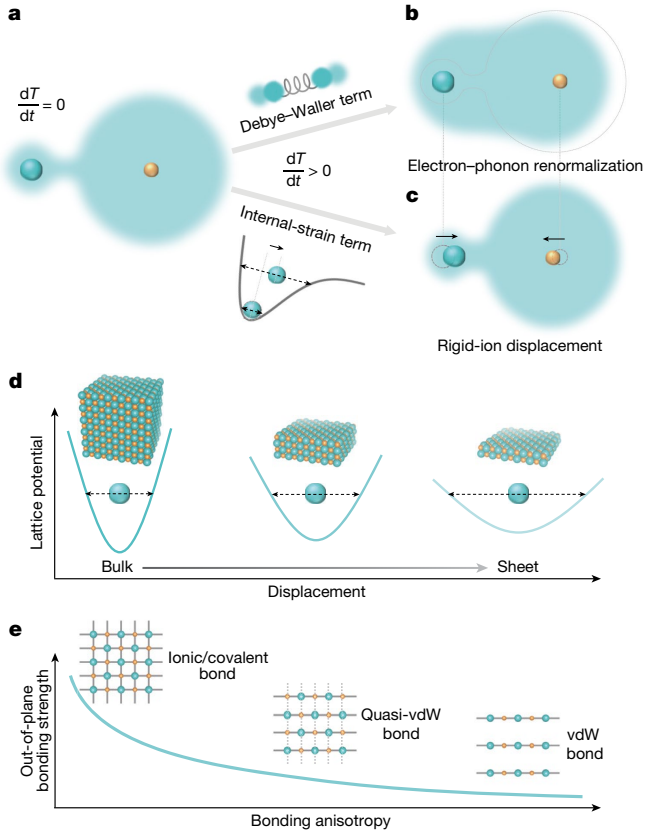

Fig. 1 | Schematics of the microscopic mechanism of the primary pyroelectricity and dimensionality effect. a–**c**, Original state (**a**) and solely contributed from $p_1^{(2)}$ (**b**) and $p_1^{(1)}$ (**c**) of ions and electron clouds (fuzzy cyan) in a crystal lattice. The schematic between **a** and **b** represents the Debye–Waller term that contributes to the electron–phonon renormalization. The lattice potential profile of an ion between **a** and **c** shows the origin of rigid-ion displacement (internal-strain term). Positive ions are in cyan and negative ones are in orange. Black arrows represent the direction of the ion displacement. The dashed shape in **b** and dashed circles in **c** represent the original shape of the electron cloud and positions of ions, respectively. Dashed arrows represent the amplitude of the ion vibration. **d**, Schematics of lattice potential profiles and ion displacements as the thickness of crystal decreases (from bulk to sheet) based on Hohenberg–Mermin–Wagner's theorem. **e**, Schematic plot of out-of-plane bonding strength as a function of bonding anisotropy in different materials. Insets show the lattices of materials with ionic/covalent bond, quasi-vdW bond and vdW bond. The out-of-plane bonding strength decreases and the bonding anisotropy increases from ionic/covalent crystal, quasi-vdW crystal to vdW crystal.

renormalization. An anharmonic-potential profile of an ion and its displacement when $dT/dt > 0$ are shown between Fig. 1a and Fig. 1c. The displacements of ions contributed solely from $p_1^{(1)}$ are shown in Fig. 1c.

Recently, the microscopic mechanisms of the pyroelectric effects in 3D and 2D materials have been revisited on the basis of first-principles calculations[13]. The contribution of the electron–phonon renormalization to pyroelectricity, which has been traditionally viewed as negligible, is found to be important. Theoretically, the 2D crystalline long-range order cannot exist within the thermodynamic limit, which is argued by Peierls based on the harmonic approximation[14], Landau based on an order-parameter expansion[15], and Hohenberg, Mermin and Wagner based on rigorous inequalities[16]. Topological defects such as dislocation pairs may stabilize a quasi-ordered (hexatic) phase and an unusual phase transition might occur in 2D systems, known as the Kosterlitz–Thouless–Halperin–Nelson–Young (KTHNY) theory[17]. A dimensional limit of a long-range-ordered crystalline phase had been expected[18], but the discovery of graphene and monolayer crystalline oxides[19] seem to defy these theorems. Debates on whether these 2D crystals can be approximated to Hohenberg–Mermin–Wagner's or KTHNY's models have been raised. Nevertheless, it is generally observed that the thermodynamic-relevant long-range order (for example, phonon) becomes less stable when approaching 2D, thereby affecting material properties[20].

For the purpose of illustration, in an extreme case, here, Hohenberg–Mermin–Wagner's theorem is applied to estimate the possible dimensionality effect of $\langle u_l^2 \rangle$. Hohenberg–Mermin–Wagner's theorem gives a finite value of $\langle u_l^2 \rangle$ in 3D and an infinite value in 2D, which is described in Supplementary Discussion 1. The physical reason leading to such prediction is that, in a 3D system, the atomic displacements are restrained by atoms from all directions, whereas in 2D, such constriction is absent. Thus, it is naturally expected that, as the thickness of a crystal decreases, there would be less restrictions for atoms to displace. In this scenario, $\langle u_l^2 \rangle$ could become larger (Fig. 1d). Hence, the pyroelectric behaviour ($p_1^{(2)}$) in 2D and free-standing nanomembranes would be very different from that in 3D.

Although conceptually illustrative, Hohenberg–Mermin–Wagner's analysis takes into account some notable assumptions, such as single element. Real materials exhibit further complexity. For example, for a non-van der Waals (non-vdW) 3D material (such as ZnO) with strong chemical bond, thinning it down by removing the strong constrictions along the out-of-plane direction would have much greater effects on its phonon dynamics and phase stability than a vdW material (such as In_2Se_3) (Fig. 1e). In fact, it has been theoretically predicted that free-standing monolayer wurtzite ZnO should not exist[21], whereas monolayer In_2Se_3 has been experimentally demonstrated widely[22]. Thus, we expect that the bonding nature along the out-of-plane direction in real materials would influence the dimensionality effect of pyroelectricity: more pronounced dimensionality effect is expected in a non-vdW system. The dimensionality effect of free-standing nanomembranes should be distinguished from the scenario in epitaxial films, which are tightly bonded on the underlying substrate, with the lattice dynamics (for example, coefficients of thermal expansion) of epilayers largely determined by the substrates. Such dimensionality effect is also different from the pyroelectricity with the dipole moment along the out-of-plane direction induced by inversion symmetry breaking at the surface or interface of materials[23,24].

Nanomembrane fabrications

In this study, we experimentally investigated the dimensionality effect of pyroelectricity in vdW, quasi-vdW and ionic/covalent pyroelectric materials. We choose β'-In_2Se_3, $CsBiNb_2O_7$ (CBNO) and ZnO as representative pyroelectric materials with vdW, quasi-vdW and ionic/covalent bonds, respectively. β'-In_2Se_3 is a room-temperature vdW ferroelectric material with an in-plane polarization of about 24 μC cm^{-2} along $\langle 11\bar{2}0 \rangle$ (calculated value)[25,26]. CBNO (space group of $P2_1am$, No. 26) is a quasi-vdW ferroelectric Dion–Jacobson phase oxide with a high T_C of about 1,033 °C (ref. [27]) and an in-plane polarization of more than 40 μC cm^{-2} along the a axis[28]. ZnO is a conventional pyroelectric material with its polarization along the c axis[29]. The unit cells of these three materials are highlighted in dashed rectangles in Fig. 2a,e,i, respectively. Here the polar axes of all three materials are parallel to the substrate surface. For pyroelectric study, we focus on the in-plane polarization mainly because the out-of-plane polarization in 2D may suffer from the depolarization field issue[30], which makes the isolation of the contribution of electron–phonon renormalization difficult. To study the dimensionality effect, free-standing crystals are preferred. It is a challenge to make truly suspended devices, so the sheets studied here are mechanically transferred ones free of strong substrate interactions.

We fabricate free-standing In_2Se_3, CBNO and ZnO sheets/nanomembranes with different thicknesses by mechanical exfoliation from a

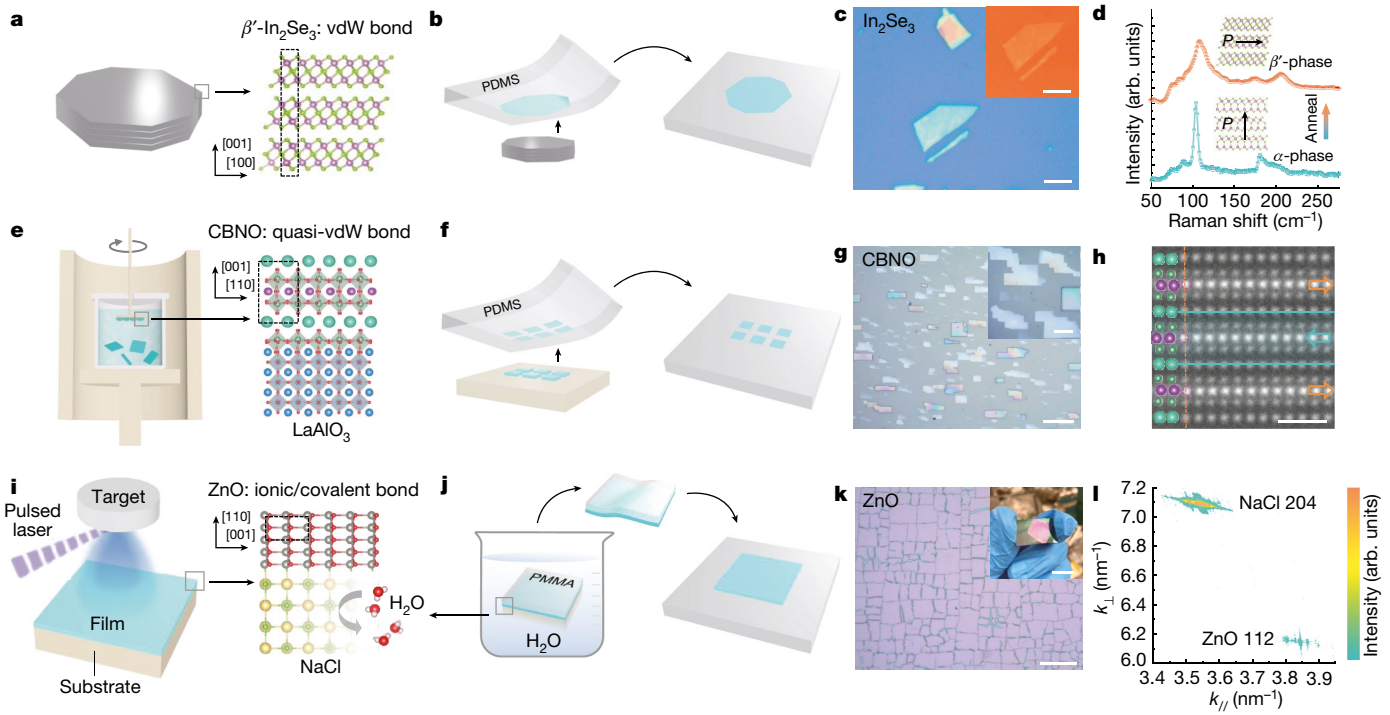

Fig. 2 | Fabrications and characterizations of sheets/nanomembranes. **a**, Schematic of a β'-In_2Se_3 bulk crystal. The atomic structure of In_2Se_3 (right panel) shows vdW bond between layers. **b**, Schematic of mechanical exfoliation (left panel) and transfer (right panel) of an In_2Se_3 sheet (cyan) by using a PDMS stamp. **c**, Optical microscopy image of a 5-unit-cell In_2Se_3 sheet transferred on a SiO_2/Si substrate. Scale bar, 5 μm. Inset is an AFM image; scale bar, 5 μm. **d**, Raman spectra of α-phase (cyan) and β'-phase (orange) In_2Se_3 at room temperature. Insets show that the α-phase has out-of-plane polarization and the β' phase has in-plane polarization. **e**, Schematic of LPE of CBNO. The substrate is $LaAlO_3$. The cross-sectional atomic structure of CBNO (right panel) shows quasi-vdW bond along the out-of-plane direction. **f**, Schematic of mechanical exfoliation (left panel) and transfer (right panel) of CBNO sheets (cyan) by using a PDMS stamp. **g**, Optical microscopy image of epitaxial sheets on the substrate. Scale bar, 50 μm. Inset is an enlarged view; scale bar, 10 μm. **h**, Cross-sectional STEM image of the CBNO sheet with [010] zone axis, showing 180° domain walls (cyan lines). The atomic model of a one-unit cell for each layer is shown on the left side. The dashed orange line and dashed purple circles are guides for the eyes. Polarization directions are indicated by orange and cyan arrows pointing to the right and left, respectively. Scale bar, 2 nm. **i**, Schematic of PLD of ZnO film. The substrate is NaCl. The cross-sectional atomic structure of ZnO (right panel) shows ionic/covalent bond. The *c*-axis of ZnO is along the in-plane direction. **j**, Schematic of dissolving NaCl in water (left panel) and transfer (right panel) of a ZnO film. **k**, Optical microscopy image of a ZnO film transferred on a SiO_2/Si substrate. Scale bar, 50 μm. Inset shows the whole centimetre-scale film; scale bar, 1 cm. **l**, RSM of as-grown ZnO film on NaCl substrate.

commercial bulk crystal (Fig. 2a,b), molten salt-assisted liquid phase epitaxy (LPE) followed by mechanical exfoliation (Fig. 2e,f) and pulsed laser deposition (PLD) followed by etching substrate away (Fig. 2i,j), respectively (see Methods). Figure 2c shows an optical microscopy image of an exfoliated In_2Se_3 sheet, with an atomic force microscopy (AFM) image in the inset. We use Raman spectroscopy to characterize its β'-phase after annealing and α-phase before annealing for comparison (Fig. 2d). Figure 2g shows an optical microscopy image of epitaxial CBNO sheets, with an enlarged view in the inset. We apply scanning transmission electron microscopy (STEM) to characterize the in-plane polarization and domain structure in CBNO (Fig. 2h). Figure 2k and its inset show optical images of a centimetre-scale ZnO film transferred on a SiO_2/Si substrate. We apply X-ray diffraction (XRD) to characterize crystallographic orientation of the film, as shown in a reciprocal space mapping (RSM) in Fig. 2l (see Methods for detailed characterizations for all three materials).

Dimensionality effect on pyroelectricity

To measure the pyroelectric coefficients in micrometre-scale sheets with different thicknesses, we use a periodic pulse technique (or Chynoweth technique[31]) (see Methods). Figure 3a shows a schematic illustration of the pyroelectric device. We fabricated sheet-based pyroelectric devices by using a dry transfer technique (see Methods) with few-layer graphene (FLG) as electrode instead of depositing metal layer to reduce the possible clamping effect from the substrate. Figure 3b–d shows optical microscopy images of representative devices for In_2Se_3, CBNO and ZnO, respectively (bottom panels), and their cross-sectional atomic models (top panels). It is observed that, immediately after the infrared (IR) laser illumination is switched from the 'ON' state to the 'OFF' state or from OFF to ON (when the illumination hits the surface of the device through the gap of the chopper blades, it is the ON state; when the illumination is blocked by the chopper blade, it is the OFF state), the pyroelectric current (and current density) ramps rapidly to a maximum absolute value and then decays in a relatively slow rate, as shown in Fig. 3e–g for devices in Fig. 3b–d, respectively. Such a result is consistent with the common observations in pyroelectric tests by the periodic pulse technique: the transition between ON and OFF states induces a large temperature fluctuation (thus, large pyroelectric current) owing to a sudden presence or removal of heat source; within consistent heating or cooling states, temperature fluctuation becomes less pronounced, leading to smaller pyroelectric response. The effective electrode area in this study is estimated by the electrode length (measured by optical microscopy, for example, Supplementary Figs. 16–18a) multiplied by the sheet thickness (measured by AFM, for example, Supplementary Figs. 16–18b,c). To improve statistics, we fabricated and measured more devices (26 in total) with different thicknesses, as shown in Supplementary Figs. 19–25 for In_2Se_3-based, Supplementary Figs. 26–35 for CBNO-based and Supplementary Figs. 36–40 for ZnO-based devices. For ferroelectric materials, all devices have been

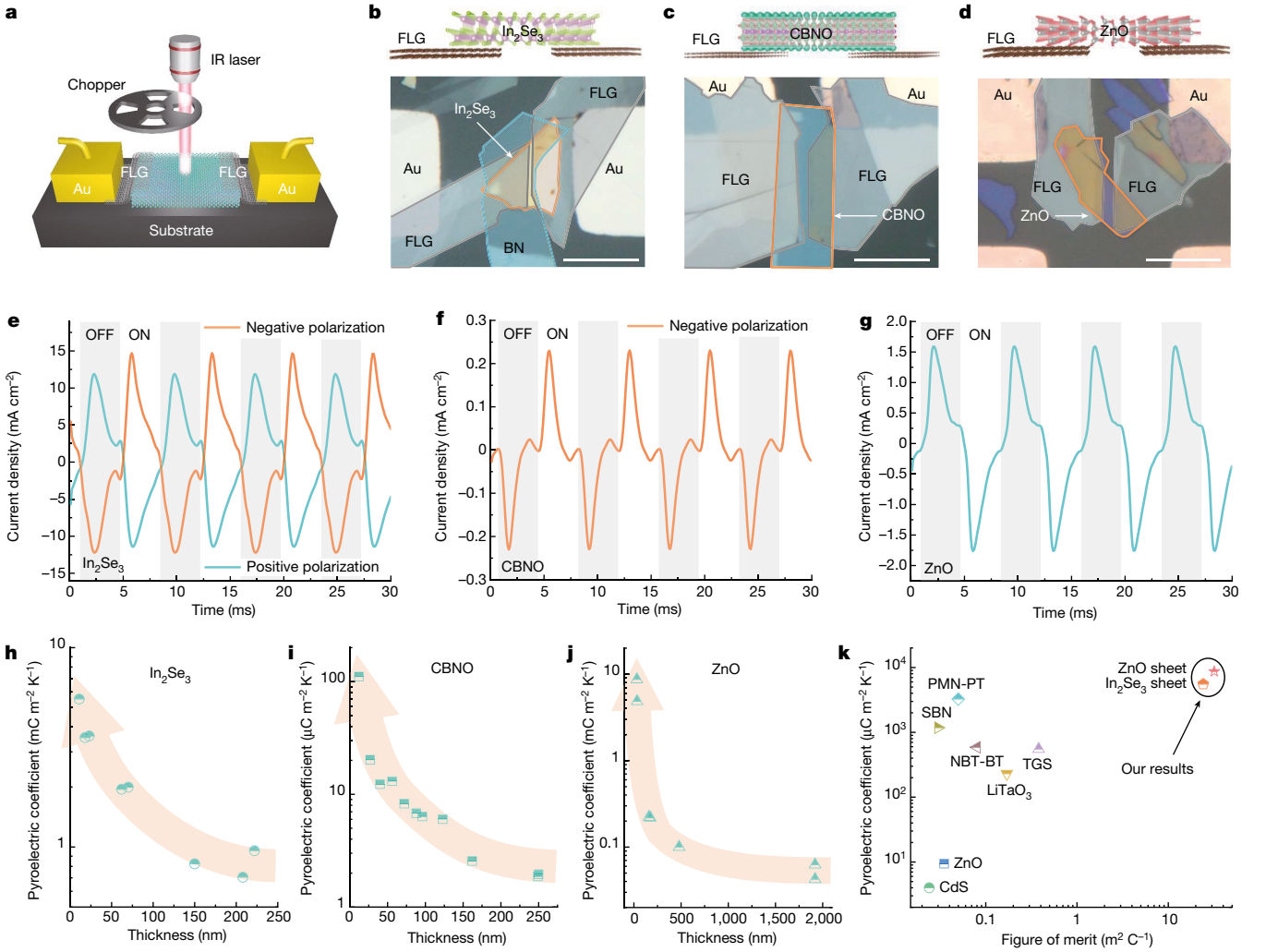

Fig. 3 | Pyroelectricity in In_2Se_3, CBNO and ZnO and the dimensionality effect. a, Schematic of the pyroelectric device model. The chopper is used to modulate the IR laser. **b**–**d**, Optical microscopy images of representative devices for In_2Se_3 (**b**), CBNO (**c**) and ZnO (**d**) (bottom panels) and their cross-sectional atomic structures (top panels). Scale bars: **b**, **d**, 10 μm; **c**, 20 μm. **e**–**g**, Pyroelectric current density under the modulated IR laser for the In_2Se_3-based device in **b** (**e**), CBNO-based device in **c** (**f**) and ZnO-based device in **d** (**g**). Orange curves in **e** and **f** are measured after positive poling and the cyan curve in **e** is measured after negative poling. **h**–**j**, Effective pyroelectric coefficients as a function of sheet thickness for In_2Se_3 (**h**), CBNO (**i**) and ZnO (**j**). Light orange arrows are guides for the eyes. **k**, Comparison of the pyroelectric coefficients and the figures of merit of In_2Se_3 (11 nm) and ZnO (32 nm) with those of conventional single-crystalline and epitaxial pyroelectric materials, including ZnO, CdS, TGS, $LiTaO_3$, PMN-PT, NBT-BT and SBN. The value is measured for TGS at 50 °C and for PMN-PT at 55 °C; values for In_2Se_3 and ZnO here are measured in the range 50–170 °C and for others are at room temperature.

poled before measurements and the direction of pyroelectric current can be switched by flipping the polarization. Indeed, we can observe the switchable pyroelectric currents after switching polarizations (positive to negative) in In_2Se_3-based devices (Fig. 3e and Supplementary Figs. 19, 21 and 24) and CBNO-based devices (Supplementary Figs. 27, 29 and 35). This switchability can rule out other possible charging scenarios, such as thermoelectric effect.

Assuming a constant pyroelectric coefficient p within a certain range of temperatures during measurements, p can be expressed by:

$$p = \frac{J\Delta t}{\Delta T} = \frac{\sigma}{\Delta T}, \quad (3)$$

in which J is the measured current density, σ is the charge density obtained by integrating J with respect to t and ΔT is the temperature change. In the current density versus time curve, usually the part corresponding to heating is chosen for extracting pyroelectric coefficients[32]. Accordingly, we calculated pyroelectric coefficients (absolute effective values) for all devices and plotted them as a function of the sheet thickness in Fig. 3h–j for In_2Se_3, CBNO and ZnO, respectively. These plots clearly show a remarkable thickness dependence of the pyroelectric coefficient in all three materials. Specifically, for In_2Se_3, the pyroelectric coefficient increases from 958.8 μC m^{-2} K^{-1} at a thickness of 222 nm to 5.5 × 10^3 μC m^{-2} K^{-1} at 11 nm; for CBNO, it increases from 2.0 μC m^{-2} K^{-1} at a thickness of 250 nm to 110.8 μC m^{-2} K^{-1} at 12 nm; and for ZnO, it increases from 42 μC m^{-2} K^{-1} at a thickness of 1,920 nm to 8.7 × 10^3 μC m^{-2} K^{-1} at 32 nm. We find that the ratios of pyroelectric coefficients between the thinnest and thickest films studied here are 6 for In_2Se_3, 55 for CBNO and 207 for ZnO. ZnO exhibits the strongest dimensionality effect and In_2Se_3 the weakest.

The figure of merit (F_v) of a pyroelectric material is often defined as $F_v = p/c_p\varepsilon_r\varepsilon_0$, in which c_p is the specific heat capacity, ε_0 is the permittivity of free space and ε_r is the relative permittivity of the pyroelectric material[33]. The c_p and ε_r for In_2Se_3 are 1.5 J K^{-1} cm^{-3} and 17, respectively[34,35], and for ZnO are 2.9 J K^{-1} cm^{-3} and 10.4, respectively[36,37] (c_p for CBNO has not been reported). Thus, we obtain a F_v of 24.2 m^2 C^{-1} for the In_2Se_3

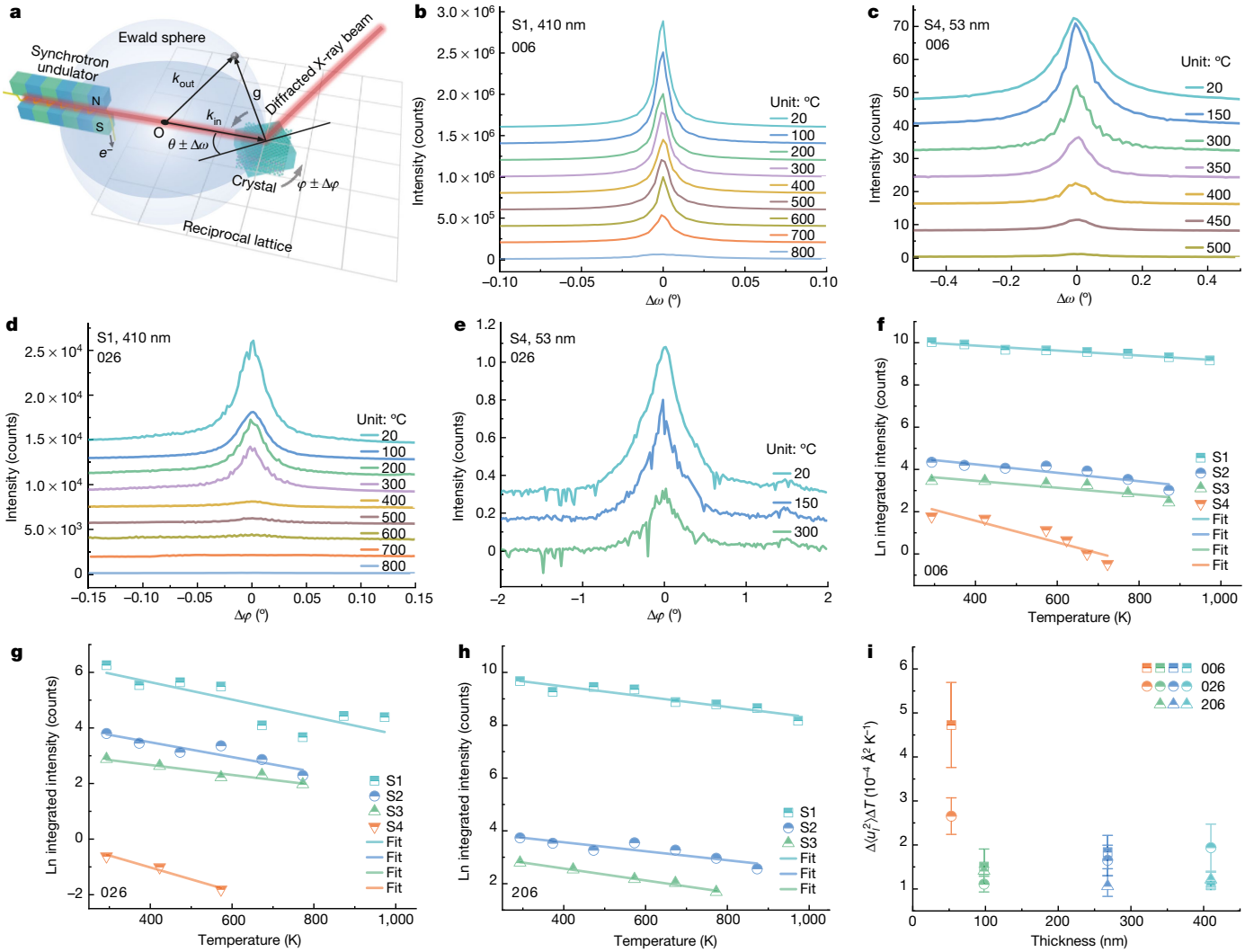

Fig. 4 | DW factor in CBNO. a, Schematic of the synchrotron XRD measurement (2θ scan and φ scan). **b**, **c**, Temperature-dependent 2θ scans of 006 reflections for CBNO sheets S1 (410 nm) (**b**) and S4 (53 nm) (**c**). **d**, **e**, Temperature-dependent φ scans of 026 reflections for sheets S1 (**d**) and S4 (**e**). Here we need to mention that the diffraction peak position for the micrometre-scale sheet is sensitive to the alignment at different temperatures. For better illustration, we normalize all peaks with respect to the peak position and present $\Delta\omega$ and $\Delta\varphi$ instead of 2θ and φ. **f**–**h**, Temperature-dependent integrated intensities (in natural logarithm) of 006 (**f**), 026 (**g**) and 206 (**h**) reflections for all sheets. Colour lines are fittings. **i**, $\triangle\langle u_l^2\rangle/\triangle T$ for reflections 006, 026 and 206 as a function of sheet thickness.

sheet with the thickness of 11 nm and 32.6 m^2 C^{-1} for the ZnO sheet with the thickness of 32 nm. Figure 3k summarizes the pyroelectric coefficients and figures of merit for In_2Se_3 (11 nm) and ZnO (32 nm) sheets, as well as most single-crystalline and epitaxial pyroelectric materials (see details in Methods). Here single crystals or epitaxial films are mainly presented, as we only focus on intrinsic pyroelectric property (polycrystalline ceramics materials or engineered interface structures (such as Au/Nb:$Ba_{0.6}Sr_{0.4}TiO_3$ (ref. [24])) are complexed by some extrinsic mechanisms, such as grain-size effects[38] and Schottky junctions[24]). The experimentally demonstrated pyroelectric coefficients for In_2Se_3 (11 nm) and ZnO (32 nm) are one to a few orders of magnitude higher than most conventional pyroelectric crystals and slightly larger than $0.79Pb(Mg_{1/3}Nb_{2/3})O_3$–$0.21PbTiO_3$ (PMN-PT). Moreover, the figures of merit for In_2Se_3 (11 nm) and ZnO (32 nm) are more than one order of magnitude larger than these conventional pyroelectric crystals.

Crystal lattice dynamics

An experimental approach to evaluate the dimensionality effect on the electron–phonon renormalization is to directly explore the DW factor of sheets of different thicknesses. The DW factor can be experimentally determined from the Bragg peak intensity measured by XRD. The intensity of a Bragg peak as a function of temperature is expressed as[39]:

$$I = I_0 e^{-G^2\langle u_l^2\rangle}, \quad (4)$$

in which $e^{-G^2\langle u_l^2\rangle}$ is the DW factor and $G = 2\pi/d$ is the reciprocal lattice vector (d is the interplanar spacing). The mean square displacement $\langle u_l^2\rangle$ is related to $\langle Q_j^2\rangle$ through $\langle u_l\rangle = \sum_j \langle Q_j\rangle \varepsilon_j/\sqrt{M_l}$, in which ε_j is the normalized Cartesian component of the eigenvector of the usual (mass-weighted) harmonic dynamical matrix and M_l is the atomic mass[40]. Thus, a stronger temperature dependence of the DW factor (or $\langle u_l^2\rangle$) reflects a larger $d\langle Q_j^2\rangle/dT$. To study the dimensionality effect on pyroelectricity (here $p_1^{(2)}$ is focused), we can measure the DW factors for sheets with different thicknesses and analyse their temperature dependencies.

In this study, we use a synchrotron X-ray source to characterize the DW factors. Figure 4a shows a schematic of the synchrotron XRD measurement. Here we use CBNO as the model system, as it has reasonable chemical and phase stability at reduced dimension at a large

temperature window under high-flux X-ray beam. We performed 2θ scans and φ scans on four CBNO sheets (samples S1, S2, S3 and S4 shown in optical microscopy images in Supplementary Fig. 46a,d,g,l, respectively) with different thicknesses (410 nm, 268 nm, 98 nm and 53 nm shown in AFM images in Supplementary Fig. 46b,c,e,f,h,i,m,n, respectively) from room temperature to 800 °C. Figure 4b,c shows temperature-dependent 006 reflections for S1 (410 nm) and S4 (53 nm), respectively. Figure 4d,e shows temperature-dependent 026 reflections for S1 and S4, respectively. 006 and 206 reflections for the other two samples S2 and S3 are shown in Supplementary Fig. 47a,b,c,d, respectively. 206 reflections for S1, S2 and S3 are shown in Supplementary Fig. 47e–g, respectively (for S4, the signal-to-noise ratio is too low to conduct conclusive analysis). We integrated all peak intensities (in natural logarithm), as shown in Fig. 4f–h for 006, 026 and 206, respectively. These results show roughly linear temperature dependencies. Their linear fittings yield values of $\Delta\langle u_l^2\rangle/\Delta T$ for all three reflections in four samples, as plotted in Fig. 4i. It clearly shows a remarkable enhancement of $\Delta\langle u_l^2\rangle/\Delta T$ for S4 (53 nm) compared with S3 (98 nm), which directly reflects an enhancement of $\mathrm{d}\langle Q_j^2\rangle/\mathrm{d}T$ and thereby a larger $p_1^{(2)}$. This enhancement of $\Delta\langle u_l^2\rangle/\Delta T$ (about 1.4 times for 026 and about 2.1 times for 006 for S4 compared with S3) is close to the enhancement (about 2 times) of our measured pyroelectric coefficients for the sheets with similar thicknesses (Fig. 3i), indicating a possible contribution of electron–phonon renormalization.

In addition, the analyses of crystal lattice dynamics based on molecular dynamics (MD) simulations with a hexagonal close-packed (HCP) solid as a toy model and temperature-dependent Raman measurements in both In_2Se_3 and CBNO also suggest that our observation of thickness-dependent pyroelectricity may have a possible correlation with the electron–phonon renormalization (see details in Methods and Extended Data Figs. 1 and 2). It is noted that, because the pyroelectric coefficient also includes the contributions from rigid-ion displacement contribution ($p_1^{(1)}$) and combined effect of piezoelectricity and thermal expansion (p_2), $p_1^{(1)}$ and p_2 could also possibly contribute to the dimensionality effect of pyroelectricity.

Conclusion

We investigated the dimensionality effect on pyroelectricity in three types of material (a vdW material In_2Se_3, a quasi-vdW CBNO and an ionic/covalent ZnO). We observed a universal large enhancement of pyroelectric coefficient in the thin sheet over a thick one. Among the three materials, ZnO shows the greatest enhancement of more than two orders of magnitude. Our measured pyroelectric coefficients and figures of merit in In_2Se_3 sheet of 11 nm and ZnO sheet of 32 nm are highest among all conventional single-crystalline and epitaxial pyroelectrics. The thickness-dependent lattice dynamics shown by MD simulations, temperature-dependent Raman spectroscopy and synchrotron XRD evidence the possible correlation between the electron–phonon renormalization and pyroelectricity. The discovery opens a window to using dimensionality-controlled pyroelectricity to design and develop high-performance sensing and energy-conversion devices.

Online content

Any methods, additional references, Nature Research reporting summaries, source data, extended data, supplementary information, acknowledgements, peer review information; details of author contributions and competing interests; and statements of data and code availability are available at https://doi.org/10.1038/s41586-022-04850-7.

1. Born, M. On the quantum theory of pyroelectricity. *Rev. Mod. Phys.* **17**, 245–251 (1945).
2. Szigeti, B. Temperature dependence of pyroelectricity. *Phys. Rev. Lett.* **35**, 1532–1534 (1975).
3. Lang, S. B. Pyroelectricity: from ancient curiosity to modern imaging tool. *Phys. Today* **58**, 31 (2005).
4. Wang, Z. et al. Light-induced pyroelectric effect as an effective approach for ultrafast ultraviolet nanosensing. *Nat. Commun.* **6**, 8401 (2015).
5. Yang, Y. et al. Pyroelectric nanogenerators for harvesting thermoelectric energy. *Nano Lett.* **12**, 2833–2838 (2012).
6. Pandya, S. et al. Pyroelectric energy conversion with large energy and power density in relaxor ferroelectric thin films. *Nat. Mater.* **17**, 432–438 (2018).
7. You, H. et al. Room-temperature pyro-catalytic hydrogen generation of 2D few-layer black phosphorene under cold-hot alternation. *Nat. Commun.* **9**, 2889 (2018).
8. Naranjo, B., Gimzewski, J. K. & Putterman, S. Observation of nuclear fusion driven by a pyroelectric crystal. *Nature* **434**, 1115–1117 (2005).
9. Stewart, J. W., Vella, J. H., Li, W., Fan, S. & Mikkelsen, M. H. Ultrafast pyroelectric photodetection with on-chip spectral filters. *Nat. Mater.* **19**, 158–162 (2020).
10. Resta, R. & Vanderbilt, D. in *Physics of Ferroelectrics: A Modern Perspective* 31–68 (Springer, 2007).
11. Allen, P. B. & Heine, V. Theory of the temperature dependence of electronic band structures. *J. Phys. C Solid State Phys.* **9**, 2305–2312 (1976).
12. Giustino, F., Louie, S. G. & Cohen, M. L. Electron-phonon renormalization of the direct band gap of diamond. *Phys. Rev. Lett.* **105**, 265501 (2010).
13. Liu, J. & Pantelides, S. T. Mechanisms of pyroelectricity in three- and two-dimensional materials. *Phys. Rev. Lett.* **120**, 207602 (2018).
14. Peierls, R. E. *Quantum Theory of Solids* 108 (Oxford Univ. Press, 1955).
15. Landau, L. The theory of phase transitions. *Nature* **138**, 840–841 (1936).
16. Halperin, B. I. On the Hohenberg–Mermin–Wagner theorem and its limitations. *J. Stat. Phys.* **175**, 521–529 (2019).
17. Kosterlitz, J. M. & Thouless, D. J. Ordering, metastability and phase transitions in two-dimensional systems. *J. Phys. C Solid State Phys.* **6**, 1181–1203 (1973).
18. Hong, S. S. et al. Two-dimensional limit of crystalline order in perovskite membrane films. *Sci. Adv.* **3**, eaao5173 (2017).
19. Ji, D. et al. Freestanding crystalline oxide perovskites down to the monolayer limit. *Nature* **570**, 87–90 (2019).
20. Xi, X. et al. Strongly enhanced charge-density-wave order in monolayer $NbSe_2$. *Nat. Nanotechnol.* **10**, 765–769 (2015).
21. Tusche, C., Meyerheim, H. L. & Kirschner, J. Observation of depolarized ZnO(0001) monolayers: formation of unreconstructed planar sheets. *Phys. Rev. Lett.* **99**, 026102 (2007).
22. Xue, F. et al. Room-temperature ferroelectricity in hexagonally layered α-In_2Se_3 nanoflakes down to the monolayer limit. *Adv. Funct. Mater.* **28**, 1803738 (2018).
23. Meirzadeh, E. et al. Surface pyroelectricity in cubic $SrTiO_3$. *Adv. Mater.* **31**, 1904733 (2019).
24. Yang, M.-M. et al. Piezoelectric and pyroelectric effects induced by interface polar symmetry. *Nature* **584**, 377–381 (2020).
25. Xu, C. et al. Two-dimensional antiferroelectricity in nanostripe-ordered In_2Se_3. *Phys. Rev. Lett.* **125**, 047601 (2020).
26. Zheng, C. et al. Room temperature in-plane ferroelectricity in van der Waals In_2Se_3. *Sci. Adv.* **4**, eaar7720 (2018).
27. Chen, C. et al. Ferroelectricity in Dion–Jacobson $ABiNb_2O_7$ (A = Rb, Cs) compounds. *J. Mater. Chem. C* **3**, 19–22 (2015).
28. Fennie, C. J. & Rabe, K. M. Ferroelectricity in the Dion-Jacobson $CsBiNb_2O_7$ from first principles. *Appl. Phys. Lett.* **88**, 262902 (2006).
29. Heiland, G. & Ibach, H. Pyroelectricity of zinc oxide. *Solid State Commun.* **4**, 353–356 (1966).
30. Junquera, J. & Ghosez, P. Critical thickness for ferroelectricity in perovskite ultrathin films. *Nature* **422**, 506–509 (2003).
31. Chynoweth, A. G. Dynamic method for measuring the pyroelectric effect with special reference to barium titanate. *J. Appl. Phys.* **27**, 78–84 (1956).
32. Lubomirsky, I. & Stafsudd, O. Invited review article: practical guide for pyroelectric measurements. *Rev. Sci. Instrum.* **83**, 051101 (2012).
33. Whatmore, R. W. Pyroelectric devices and materials. *Rep. Prog. Phys.* **49**, 1335–1386 (1986).
34. Boehnke, U. C., Kühn, G., Berezovskii, G. A. & Spassov, T. Some aspects of the thermal behaviour of In_2Se_3. *J. Therm. Anal.* **32**, 115–120 (1987).
35. Wu, D. et al. Thickness-dependent dielectric constant of few-layer In_2Se_3 nanoflakes. *Nano Lett.* **15**, 8136–8140 (2015).
36. Newnham, R. E. *Properties of Materials: Anisotropy, Symmetry, Structure* (Oxford Univ. Press, 2005).
37. Langton, N. H. & Matthews, D. The dielectric constant of zinc oxide over a range of frequencies. *Br. J. Appl. Phys.* **9**, 453–456 (1958).
38. Zhao, Z. et al. Grain-size effects on the ferroelectric behavior of dense nanocrystalline $BaTiO_3$ ceramics. *Phys. Rev. B* **70**, 024107 (2004).
39. Warren, B. E. *X-ray Diffraction* (Courier Corporation, 1990).
40. Liu, J., Fernández-Serra, M. V. & Allen, P. B. First-principles study of pyroelectricity in GaN and ZnO. *Phys. Rev. B* **93**, 081205 (2016).

Methods

Liquid phase epitaxial growth of CBNO sheets

We chose $LaAlO_3$ (LAO) as the substrate for epitaxial growth of CBNO. The lattice mismatches between CBNO and LAO are about 4.1% for in-plane CBNO[100]‖LAO[100] with two CBNO unit cells matching three LAO unit cells and about 1.7% for in-plane CBNO[100]‖LAO[110] (obtained from the lattice parameters of orthorhombic CBNO, a = 5.495 Å, b = 5.423 Å, c = 11.38 Å and cubic LAO above 435 °C, a = 3.821 Å). Before growth, we cleaned a LAO substrate (MTI Corporation) with acetone, ethanol and ultra-pure water in an ultrasonic bath for 5 min successively and then blew it with dry air. CsCl (Sigma-Aldrich, 99.9%) is used as the molten salt and precursors include Cs_2CO_3 (Sigma-Aldrich, 99%), Bi_2O_3 (Sigma-Aldrich, 99.9%) and Nb_2O_5 (Sigma-Aldrich, 99.9%), with a molar ratio of 3:2:4. For the growth, we constructed two set-ups: horizontal system (horizontal furnace) and vertical system (vertical furnace). The horizontal system is more convenient to grow small and thin sheets with a low weight ratio between the CsCl molten salt and precursors, whereas the vertical system is more effective for preparing large and thick sheets with a relatively high weight ratio. In the horizontal furnace set-up, the LAO substrate was placed flat at the bottom of a crucible and the weight ratio of molten salt to precursors was varied from 50:1 to 500:1. The temperature was increased to 200 °C and held for 2 h to dry all powders. Then it was increased to 600 °C and held for 2 h to decompose Cs_2CO_3 into Cs_2O. Subsequently, the temperature was increased to 900 °C, held for 4 h and gradually decreased to room temperature with a cooling rate of 2 °C min^{-1}. In the vertical furnace set-up, the LAO substrate was placed vertically and tied by a Pt wire. The weight ratio of CsCl molten salt to all precursors was varied from 10:1 to 50:1. The temperature was increased to 200 °C and held for 2 h to dry all powders. After the decomposition of Cs_2CO_3 at 600 °C for 2 h, the temperature was increased to 850 °C for 4 h to fully melt all precursors and then suddenly decreased to 750 °C. Then the vertically hung LAO substrate was lowered into the crucible and immerged into molten salt for 2 h. Finally, the LAO substrate was pulled out directly from the solution using the Pt wire and gradually cooled down to room temperature for further characterizations.

Pulsed laser deposition of ZnO thin films

We choose NaCl as the substrate for epitaxial growth of ZnO thin films. The lattice mismatch between ZnO and NaCl is 5.6% for in-plane ZnO[001]‖NaCl[100]. We obtained a fresh NaCl substrate by cleavage and then immediately loaded it into the growth chamber to avoid possible surface degradation. Before growth, the vacuum chamber was evacuated to about 10^{-5} mbar and then a O_2 gas flow (99.999%) was introduced into the chamber. A KrF excimer laser (wavelength of 248 nm) with a power of 150 mJ and a frequency of 5 Hz was used to ablate the ZnO target. We maintained the substrate temperature at 200 °C, 300 °C and 400 °C and pressure at about 5 mbar during the growth. We varied the growth time from 2 mins to 120 mins. Thus, ZnO epitaxial films with different thicknesses were fabricated.

Fabrication and transfer of free-standing sheets

To fabricate In_2Se_3 and CBNO sheets, we used a polydimethylsiloxane (PDMS) stamp to press a bulk In_2Se_3 crystal (HQ Graphene) and an epitaxial CBNO/LAO sample, respectively, and then quickly removed the PDMS. Owing to the layered nature of both In_2Se_3 and CBNO, sheets could be exfoliated and attached on the PDMS. To obtain ultra-thin sheets, we pressed two PDMS stamps with thick sheets together and exfoliated a few times. Finally, we could transfer these sheets on any substrate by pressing the PDMS and then slowly removing it. The β'-In_2Se_3 sheets/crystals were obtained by annealing the α-In_2Se_3 sheets/crystals at 300 °C. To fabricate ZnO sheets, we first coated a poly(methyl methacrylate) (PMMA) film on the ZnO/NaCl sample as a supporting layer by spin coating. Then we placed the PMMA/ZnO/NaCl sample in water. After the NaCl substrate was fully dissolved, we picked up the floating PMMA/ZnO film by using a Si wafer. Finally, a free-standing ZnO film was obtained after removing the PMMA layer using acetone. By using a PDMS stamp, we can break the film into sheets and transfer the sheets onto any substrate.

Device fabrication

We used mask-less lithography (Intelligent Micro Patterning model SF-100 Lightning Plus, positive photoresist S1813) to draw patterns on a substrate (blue glass, an IR absorber for pyroelectric measurements) with the channel distance of approximately 10–30 μm. Then we deposited Ti (3 nm)/Au (20 nm) layers on the patterned substrate by using e-beam evaporation. We used FLG as electrical contacts. FLG was fabricated using the same method for fabrication of In_2Se_3 sheets. We loaded the PDMS stamps with In_2Se_3 sheets, CBNO sheets, ZnO sheets or FLGs onto a three-axis micromanipulator. Then we aligned the sheets to the Ti/Au patterned substrate under an optical microscope. Using the three-axis micromanipulator, we gently attached the sheets into the desired position and then gently released the PDMS stamp. After that, the sheets were left on the substrate. In this way, pyroelectric devices with FLGs as contacts were fabricated. For In_2Se_3, the polar direction is probably perpendicular to the edge of a triangle sheet. For CBNO, it is at 45° with respect to the edge of a rectangle sheet. For ZnO, it is along the [001] direction (one edge of the film). To ensure a polar component along the current direction, we aligned the channels of most CBNO-based and In_2Se_3-based devices to be roughly parallel to the edges of sheets and the channels of ZnO-based devices at about 45° with respect to one edge of the film.

X-ray diffraction

We performed XRD measurements by using a PANalytical X'Pert PRO MPD system with a Cu Kα source and a PIXcel solid-state line detector. ω–2θ scans were acquired with a divergent-beam Bragg–Brentano geometry over a large 2θ range from 5° to 90° to detect small inclusions of possible secondary phases or misoriented grains. ω-rocking curves were obtained using a constant 2θ angle corresponding to the CBNO 004 reflection and using a parallel-beam geometry with a hybrid mirror and a two-bounce two-crystal Ge(220) monochromator, yielding a parallel incident beam with a wavelength $\lambda_{K\alpha1}$ = 1.5406 Å, a divergence of 0.0068° and a width of 0.3 mm (ref. [41]). We obtained XRD pole figures and φ-scans by using a point-focus optics with a poly-capillary X-ray lens that provides a quasi-parallel Cu Kα beam to minimize defocusing effects associated with the non-uniform sample height owing to the sample tilt.

Synchrotron X-ray scattering

Synchrotron XRD measurements of the CBNO single-crystal-sheet samples to quantitatively extract the DW factor information were performed on a six-circle Newport Kappa diffractometer in the beamline 33-ID-D at Advanced Photon Source, Argonne National Laboratory[42]. The total X-ray flux is about 2.0×10^{12} photons s^{-1}. The X-ray beam was focused by a pair of Kirkpatrick–Baez mirrors down to a beam profile of about 20 μm (vertical) × 40 μm (horizontal) to collect sufficient diffraction signal out of the small size thin CBNO single crystal. The XRD measurements were carried out using an X-ray energy of 20 KeV. The 2D diffraction images at the out-of-plane L direction in the reciprocal space were taken by a pixel array area detector (Dectris PILATUS 100K). These images were used to properly remove the diffuse scattering background for data reduction. The temperature-dependent XRD measurements were performed an Anton Paar Domed DHS 1100 heating stage mounted onto the Newport six-circle diffractometer. The heating measurements were carried out in open-air condition.

Microscopical characterizations

We characterized the morphology of sheets and films by using a Nikon Eclipse Ti-S inverted optical microscope. We used a multimode TM

atomic force microscope to check the flatness and obtain the thickness of sheets with a tapping mode. The high-resolution TEM image and electron diffraction pattern of the CBNO sheet were collected with a FEI F20 TEM operated at 200 kV. High-angle annular dark-field Cs-corrected STEM images were acquired on a fifth-order aberration-corrected 300-keV FEI Titan Themis with a probe convergence semiangle of 21.4 mrad and inner and outer collection angles of 68 mrad and 340 mrad, respectively. We obtained vibration modes of the In_2Se_3, CBNO and ZnO sheets from a Raman spectrum collected by using a WITec alpha300 confocal Raman microscope with an excitation source of CW 532 nm.

Second-harmonic generation

We measured rotational anisotropy second-harmonic generation (RA-SHG) by using a home-made system (Keopsys KPS-BT2-YFL-1083-40-COL 1,083-nm 3-W CW fibre laser, Thorlabs 4 Megapixel Monochrome Scientific CCD Camera, Princeton Instruments SP-2358 spectrograph and Nikon Eclipse Ti-S optical microscope). We use a 1,064-nm 1/2 waveplate (Thorlabs, 25.4 mm, Mounted Zero Order 1/2 Waveplate 1,064 nm) to rotate the polarization direction of our laser and a polarizer (Thorlabs, Visible Wire Grid Polarizers: 420–700 nm) to select the SHG signals with a polarization direction parallel to the (110) direction of a CBNO sheet.

Electron backscatter diffraction

We performed electron backscatter diffraction (EBSD) to obtain the spatial crystallographic orientation map, pole figure and inverse pole figure. The detector is a NordlysNano detector from Oxford Instruments, integrated in a Carl Zeiss Ultra 1540 EsB SEM-FIB system. A 10-kV electron beam was used for the EBSD characterization; the sample was tilted at 70° relative to the incident electron beam, with a working distance of 20.0 mm. The crystallographic orientation data were collected and analysed by the Aztec software from Oxford Instruments. The surface scan area was set at 40 × 36 μm in size, with a scan step of 1.0 μm.

Reflection high-energy electron diffraction

For reflection high-energy electron diffraction (RHEED) characterization of the near-surface structure of sheets, the CBNO sheets transferred on Si(100) substrate was loaded into a high-vacuum chamber equipped with RHEED apparatus. The incident energy and incident angle of the electron beam are 9 keV and roughly 1°, respectively.

Transport measurements

For pyroelectric measurements of sheet-based devices, we used a periodic pulse technique. The IR laser beam was generated from a DILAS M1F4S22-1064 fibre-coupled diode laser with a central wavelength of 1,064 nm. The beam was focused by two long-focus convex lenses and the 20× objective lens of an optical microscope. A laser spot with a diameter of about 100 μm was shone onto the microdevice. To generate periodic heating cycles to induce the pyroelectric current, the laser beam was chopped at 133 Hz. A Stanford Research SR830 DSP lock-in amplifier onto which the chopper was connected as a reference signal was used to record the pyroelectric signal.

Supplementary Figure 13 shows a schematic of the pyroelectric measurement. Basically, the optical path of a high-power CW IR laser is spatially modulated by an external optical chopper. By programming the frequency of the chopper, the laser illumination is periodically blocked and allowed to hit the surface of the pyroelectric device, yielding periodic cooling and heating with controlled duration on the device. With lock-in amplification, such a set-up results in measurable pyroelectric currents, even in the micrometre-scale sheet. To evaluate the temperature, we track the change of the resistance of a thin Ni stripe (roughly 20 nm) under laser heating. Through the temperature coefficient of its resistance, we can calibrate the temperature change at the substrate surface, as shown in Supplementary Figs. 14 (circuit diagram) and 15a–d (measurements) (see Supplementary Discussion 6).

Molecular dynamics simulation

We designed a simple molecular model of HCP solid to understand the effect of interlayer bonding strength. There are six atomic species in this HCP model. Species A, B and C constitute hexagonally closed-packed *A* layer, whereas species D, E and F constitute the hexagonally closed-packed *B* layers, as shown in Supplementary Fig. 48a. Within each layer, atoms bond strongly to the other two species, whereas they repel the same species, such that a monolayer HCP solid is thermodynamically stable, by the balance of the attractive intralayer hetero-bond and repulsive intralayer homo-bond. The interaction across layers is always attractive, varying from the intralayer hetero-bond strength (thus corresponding to bulk HCP crystal) to half of that. The particle–particle interaction is described by a modified Lennard-Jones (LJ) potential that we refer to as bump Lennard-Jones (BLJ) potential:

$$\phi_{\mathrm{LJ}}(r) = 4\varepsilon_{\alpha\beta}\left(\frac{\sigma_{\alpha\beta}^{12}}{r^{12}} - \frac{\sigma_{\alpha\beta}^{6}}{r^{6}}\right) - 4\varepsilon_{\alpha\beta}\left(\frac{\sigma_{\alpha\beta}^{12}}{r_{\alpha\beta,c}^{12}} - \frac{\sigma_{\alpha\beta}^{6}}{r_{\alpha\beta,c}^{6}}\right)$$

$$\phi_{\mathrm{BLJ}}(r) = \begin{cases} \phi_{\mathrm{LJ}}(r), & r < r_{\alpha\beta,s} \\ \phi_{\mathrm{LJ}}(r) + \varepsilon_B\varepsilon_{\alpha\beta}\cdot\sin^2\left(\pi\dfrac{r_{\alpha\beta,c}-r}{r_{\alpha\beta,c}-r_{\alpha\beta,s}}\right), & r_{\alpha\beta,s} \le r < r_{\alpha\beta,e}. \\ \phi_{\mathrm{LJ}}(r), & r > r_{\alpha\beta,e} \end{cases}$$

Here $\phi_{\mathrm{LJ}}(r)$ is the conventional truncated LJ potential, with $\varepsilon_{\alpha\beta}$ and $\sigma_{\alpha\beta}$ providing the energy and length scales, respectively, and $r_{\alpha\beta,c}$ providing the cut-off. $\phi_{\mathrm{BLJ}}(r)$ includes an extra energy penalty term between $r_{\alpha\beta,s}$ and $r_{\alpha\beta,e}$, with a bump height of $\varepsilon_B\varepsilon_{\alpha\beta}$. The potential parameter is shown in Supplementary Table 1. Supplementary Figure 48b shows potential energy as a function of atomic separation for intralayer homo-bond (blue), intralayer hetero-bond (red) and interlayer bonds (green). The energy and length units are chosen as $\varepsilon_{\mathrm{e}} = 0.5\varepsilon_{AB}$ and $\sigma_0 = \sigma_{AB}$ for convenience. All particles have identical mass of m_0. The time unit is $t_0 = \sigma_0\sqrt{m_0/\varepsilon_{\mathrm{e}}}$. The equations of motion are numerically integrated using the velocity Verlet algorithm with a time step of $0.005t_0$. The samples are between 10 and 32 layers in thickness. Each layer is about $0.91\sigma_{AB}$ in thickness. The lateral dimensions of the samples are about $67\sigma_{AB}$ by $68\sigma_{AB}$ with periodic boundary conditions. Initial structures are relaxed in Nose-Hoover isothermal–isobaric ensemble to relax the in-plane stresses. Atomic displacement data were collected under canonical ensemble with a temperature of $0.15\varepsilon_{AB}/k$ controlled by a Nose–Hoover thermostat for a duration of $0.25M\,t_0$. In-plane and total mean square displacements are calculated using the atomic positions from the second half ($0.125M\,t_0$) of the trajectory.

Epitaxy growth and structural characterizations

To investigate the intrinsic in-plane pyroelectricity, single-crystalline or epitaxial samples are desirable. The In_2Se_3 sheet fabricated by mechanical exfoliation can inherit the high crystallinity of the bulk crystal. Figure 2c shows an optical microscopy image of an exfoliated sheet with an AFM image in the inset. We use Raman spectroscopy to characterize its phase. Figure 2d shows the Raman spectra of an as-transferred sheet after annealing (top, orange) and the sheet before annealing (bottom, cyan) for comparison. For the bottom spectrum, the peak positions at about 90 cm^{-1}, 104 cm^{-1} and 180 cm^{-1} can be assigned to E^2, A_1^1 and E^4 phonon modes, respectively, of α-In_2Se_3 (refs. [43,44]). For the top spectrum, the peak positions at about 109 cm^{-1}, 175 cm^{-1} and 206 cm^{-1} can be attributed to the phonon modes of β'-In_2Se_3 (refs. [44,45]).

LPE provides high-quality epitaxial films or sheets and it is suitable for the preparation of complex oxides[46]. We chose LAO as substrate for the epitaxial growth of CBNO sheets owing to their relatively small lattice mismatch (about 1.7% for in-plane CBNO[110]‖LAO[100] and 4.1% for in-plane CBNO[100]‖LAO[100]). The right panel of Fig. 2e shows

a schematic of the cross-sectional atomic structure of CBNO/LAO. Figure 2g shows an optical microscopy image of epitaxial CBNO sheets, with an enlarged view in the inset. The sheets distribute regularly on the LAO substrate with their main four edges parallel to those of the substrate, respectively, implying an epitaxial growth. Further, we grew large epitaxial sheets with a side length of about 200 μm and free-standing sheets with sizes up to a millimetre, as shown in Supplementary Fig. 1a,b, respectively. Scanning electron microscopy and AFM images in Supplementary Fig. 2a–e, respectively, show morphology of as-grown individual sheets. Owing to the layered nature of CBNO, we can obtain free-standing ultra-thin sheets (few layers down to monolayer) by mechanical exfoliation, as shown in Supplementary Fig. 3a–e. We observed screw dislocations on the surface of the sheets from the AFM images in Supplementary Fig. 4a–c, showing that LPE has a low supersaturation, leading to a screw-dislocation-driven growth mode[47,48] (see Supplementary Discussion 1).

We conducted XRD and aberration-corrected STEM to characterize the crystallinity of epitaxial CBNO sheets on LAO and the epitaxial relationship, as discussed in Supplementary Discussion 3 and shown in Supplementary Fig. 5a–c. Further, we characterized the symmetry and structure of an individual sheet by RA-SHG, EBSD and RHEED, as shown in Supplementary Figs. 6, 7a–e and 8a–f, respectively (see Supplementary Discussion 3 and Supplementary Table 2). Also, by using transmission measurement, we estimated the bandgap of CBNO, which is about 3.64 eV (see Supplementary Fig. 9 and Supplementary Discussion 4).

As a ferroelectric material, ferroelastic domains are naturally formed, which can be characterized by STEM and TEM[49]. The cross-sectional STEM image of a CBNO sheet (zone axis of [010]) with assigned atoms in Fig. 2h clearly shows in-plane polarization directions pointing to the left (cyan arrow) and right (orange arrows). These directions correspond to different Bi ion displacements (dashed purple circles and a dashed orange line are guides for the eyes). We can find two kinds of domains and 180° (parallel) domain walls (horizontal cyan lines). TEM images in Supplementary Fig. 10a,b and a diffraction pattern in Supplementary Fig. 10c (zone axis of [001]) clearly show periodical domain stripes and spots splitting, respectively. The spots splitting could be originated from two domains with an in-plane rotation of 90° from each other (*a*–*a* domains)[50]. We can also observe the spot splitting in a fast Fourier transform (FFT) image (Supplementary Fig. 10e) transformed from a STEM image (zone axis of [001], Supplementary Fig. 10d). Supplementary Figure 10f shows an inverse FFT from the FFT, with white spots highlighting the lattice for one domain, resulting in one domain with a perfect atomic structure and the other domain being slightly distorted. It clearly shows a 90° domain wall. The domain wall is along {110} planes, as sketched in the atomic model of Supplementary Fig. 10g. Such domain arrangements (orthogonal and parallel) help to alleviate electrostatic energy and spontaneous strains. Details of ferroelastic domains are discussed in Supplementary Discussion 5.

For ZnO, free-standing sheets cannot be fabricated by mechanical exfoliation because it is a non-vdW material. Here we fabricated free-standing ZnO films by using a water-soluble substrate NaCl for epitaxial growth, followed by etching NaCl through water. Optical microscopy images in Supplementary Fig. 11a–d show the morphology of epitaxial films with different thicknesses. We can observe aligned wrinkles in thin films (32 nm) and cracks in thick films (160–1,920 nm). These wrinkles and cracks could be originated from the large difference of thermal expansion coefficients between ZnO (1.57×10^{-5} K^{-1})[51] and NaCl (4.0×10^{-5} K^{-1})[52]. Optical microscopy images in Fig. 2k show a centimetre-scale film transferred on a SiO_2/Si substrate. We conducted XRD measurements to study the crystallographic orientation of the film and its epitaxial relationship to the substrate. 2θ scans (changing the diffraction angle) in Supplementary Fig. 12a show that the film grows along the [110] direction (the out-of-plane epitaxial relation is ZnO(110)||NaCl(001)). The RSM in Fig. 2l and φ scans (rotating the sample around its normal direction at a fixed diffraction angle) in Supplementary Fig. 12b,c show that the in-plane epitaxial relationship is ZnO[001]||NaCl[100] (note that two equivalent perpendicular domains exist and the lattice mismatch between ZnO(002) and NaCl(100) is 5.6%) and this epitaxial film (160 nm) is fully relaxed. 2θ scans in Supplementary Fig. 12d confirm the same out-of-plane reflection (110) in the transferred film as the as-grown one.

Pyroelectric materials

The single-crystalline and epitaxial pyroelectric materials shown in Fig. 3k are ZnO (ref. [29]), GaN (ref. [53]), CdS (ref. [54]), triglycine sulfate (TGS)[55], $LiTaO_3$ (ref. [33]), $LiNbO_3$ (ref. [56]), $PbTiO_3$ (ref. [57]), PMN-PT[58], Mn:0.946$Na_{0.5}Bi_{0.5}TiO_3$–0.054$BaTiO_3$ (NBT-BT)[59] and $Sr_{0.5}Ba_{0.5}Nb_2O_6$ (SBN)[60].

Crystal lattice dynamics

The pyroelectric coefficient is directly related to lattice dynamics in pyroelectric crystals, as described in equation (2). To understand the effects of out-of-plane bonding strength and sheet thickness on lattice dynamics, with a HCP solid as a toy model, we carried out a series of MD simulations (see earlier section). We focus on the relation between mean square displacement $\langle u_l^2 \rangle$ and out-of-plane bonding strength/sheet thickness. The use of the HCP model rather than the real materials allows us to simulate a sheet with large enough lateral size that is needed for the observation of substantial dimensionality effect on phonon dynamics[61]. Supplementary Videos 1–6 show the animations of the simulated results with the lattice vibrations of the sheet tuned by varied thickness and out-of-plane bonding strength. Extended Data Figure 1a shows the $\langle u_l^2 \rangle$ only in in-plane directions as a function of step time in sheets of 32 layers (left), 16 layers (middle) and ten layers (right). As the thickness decreases, the in-plane $\langle u_l^2 \rangle$ increases for both out-of-plane bonding strengths of ε_e and $\varepsilon_e/2$. In Extended Data Fig. 1b, we plotted the average in-plane $\langle u_l^2 \rangle$ in all three types of sheet as a function of the thickness and out-of-plane bonding strength. In Extended Data Fig. 1c, their percentage changes versus thickness are plotted. For the case of out-of-plane bonding strength ε_e, the in-plane $\langle u_l^2 \rangle$ for the ten-layer sheet shows an enhancement of (8.7 ± 1.9)% compared with 32 layers, whereas for the case of $\varepsilon_e/2$, it shows an enhancement of (3.9 ± 1.3)%. These simulation results evidence the dimensionality effect on mean square displacement, which is more pronounced in sheets with stronger out-of-plane bonding strength. The total $\langle u_l^2 \rangle$ also shows a similar phenomenon (Supplementary Fig. 41a–c). It is noted that further reducing the out-of-plane bonding strength or thickness within this model system could markedly affect its structural stability.

Despite the use of computationally large supercells in our MD simulations, the MD supercells only qualitatively characterize the dimensionality effect. This is because experimentally accessible samples are much larger in size and more complex in chemistry. Thus, experimental investigations are needed to understand the thickness-dependent and bonding-strength-dependent lattice dynamics. The phonon dynamics in classical ferroelectric perovskites has been widely investigated by Raman spectroscopy[62]. Hence, we conducted Raman measurements on free-standing In_2Se_3, CBNO and ZnO sheets. Supplementary Figures 42a–f and 43a–j show optical microscopy and AFM images, and temperature-dependent Raman spectra for In_2Se_3 and CBNO sheets, respectively. Supplementary Figure 44a,b shows an optical microscopy image and Raman spectra for ZnO sheets (temperature-dependent measurements are not performed on ZnO sheets owing to the low Raman signal). To investigate the dimensionality effect, we measured two types of sample (thick and thin) for comparison for each material. The thicknesses of thick and thin sheets are respectively 280 nm and 29 nm for In_2Se_3 and 730 nm and 35 nm respectively for CBNO. Here we focus on the phonon with a frequency of about 109 cm^{-1} for In_2Se_3 and the phonon with a frequency of about 585 cm^{-1} for CBNO, as shown in Extended Data Fig. 2a,b, respectively. The phonon at approximately 109 cm^{-1} for In_2Se_3 could be assigned to the A_g^2 mode[43] and the phonon at approximately 585 cm^{-1} for CBNO could be attributed to a small distortion of NbO_6

octahedra along the in-plane direction[63] (in-plane phonon, as schematically illustrated in the inset of Extended Data Fig. 2f).

Extended Data Figure 2c,f plots peak positions of the A_g^2 phonon of In_2Se_3 and the in-plane phonon of CBNO, respectively, at different temperatures. Both phonons show a decreasing frequency with increasing temperature in both thick and thin sheets. The temperature-dependent shift of the phonon frequency mainly originates from the thermal expansion of the lattice and phonon–phonon interactions[64,65]. The phonon frequency at temperature T above room temperature (293 K) can be written by the first-order approximation as[64–66]:

$$\begin{aligned}\omega(T) &= \omega_0 + \Delta\omega_e(T) + \Delta\omega_d(T) \\ &\approx \omega(293) + k_e(T-293) + k_d(T-293),\end{aligned} \quad (5)$$

in which ω_0 is the frequency of phonon mode in a perfect harmonic lattice, $\Delta\omega_e(T)$ represents the frequency shift due to the thermal expansion of lattice[67], $\Delta\omega_d(T)$ represents the frequency shift due to the phonon decay into phonons with lower energy[65], and k_e and k_d are the linear slopes of the first-order approximation of the thermal expansion and phonon decay contributions, respectively. The detailed discussion of $\Delta\omega_e(T)$ and $\Delta\omega_d(T)$ is presented in Supplementary Discussion 7. The experimental temperature-dependent frequencies of both phonons (In_2Se_3 and CBNO) for both thick and thin sheets can be linearly fitted by the first-order approximation equation (5), yielding $k_e + k_d$ of $-(7.64 \pm 0.98) \times 10^{-3}$ cm^{-1} K^{-1} and $-(1.79 \pm 0.21) \times 10^{-2}$ cm^{-1} K^{-1} for the A_g^2 phonon in the thick and thin In_2Se_3 sheets, respectively, and $-(1.22 \pm 0.12) \times 10^{-2}$ cm^{-1} K^{-1} and $-(3.17 \pm 0.26) \times 10^{-2}$ cm^{-1} K^{-1} for the in-plane phonon in the thick and thin CBNO sheets, respectively. For In_2Se_3, the thin sheet shows a larger slope (enhancement of 134.3%) of the A_g^2 phonon shift than the thick one. For CBNO, the thin sheet shows a larger slope (enhancement of 159.8%) of the in-plane phonon shift than the thick one.

Extended Data Figure 2d,g shows the full width at half maximums (FWHMs) of the A_g^2 phonon of In_2Se_3 and the in-plane phonon of CBNO, respectively. Both phonons show increasing FWHM values with increasing temperature in both thick and thin sheets. Usually, the phonon damping is probably caused by the phonon confinement, defect scattering and residual stress[68]. Here, as both In_2Se_3 and CBNO samples are single crystals with low defects, the observed phonon damping may mainly originate from the phonon–phonon interactions[64,65]. By the first-order approximation (linear fitting), slopes of $(3.54 \pm 0.27) \times 10^{-2}$ cm^{-1} K^{-1} and $(5.92 \pm 0.22) \times 10^{-2}$ cm^{-1} K^{-1} are obtained for the A_g^2 phonon in the thick and thin In_2Se_3 sheets, respectively, and slopes of $(1.58 \pm 0.17) \times 10^{-2}$ cm^{-1} K^{-1} and $(4.35 \pm 0.48) \times 10^{-2}$ cm^{-1} K^{-1} are obtained for the in-plane phonon in the thick and thin CBNO sheets, respectively. For both In_2Se_3 and CBNO, the thin sheet shows a larger slope of phonon damping compared with the thick one, indicating a substantial contribution from phonon–phonon interactions. The slope enhancement for the thin sheet compared with the thick one for CBNO is 175.3%. The slope enhancement for In_2Se_3 is 67.2%. This observation implies that the large slope enhancement ($k_e + k_d$) for the phonon frequency in Extended Data Fig. 2c,f is largely a result of phonon–phonon interactions (k_d). It is noted that the enhancements of phonon softening and damping for the approximately 933-cm^{-1} phonon in the thin CBNO sheet compared with the thick one are smaller, as shown in Supplementary Fig. 45a–d and discussed in Supplementary Discussion 7.

According to equation (2), the second-order primary pyroelectricity $p_1^{(2)}$ is directly related to the mean square amplitude of normal modes and its temperature derivative $d\langle Q_j^2\rangle/dT$. Here $\langle Q_j^2\rangle$ can be expressed by[13]

$$\langle Q_j^2\rangle = \frac{\hbar}{2}\frac{2n_j+1}{\omega_j}, \quad (6)$$

in which ω_j is the phonon eigenfrequency and n_j is the Bose–Einstein distribution function. Here, for simple estimations, we use the measured phonon frequency to represent ω_j. Extended Data Figure 2e,h plots $\langle Q_j^2\rangle$ of the A_g^2 phonon of In_2Se_3 and the in-plane phonon of CBNO, respectively, as a function of temperature for both thick and thin sheets. Linear fittings yield slope enhancements of 5.1% (from 1.38×10^{-30} eV s^2 K^{-1} to 1.45×10^{-30} eV s^2 K^{-1}) for the A_g^2 phonon of In_2Se_3 and 280% (from 6.62×10^{-34} eV s^2 K^{-1} to 25.20×10^{-34} eV s^2 K^{-1}) for the in-plane phonon of CBNO for the thin sheet compared with the thick one.

It is technically difficult to use Raman measurements to access all $\langle Q_j^2\rangle$ and not all modes contribute substantially to the pyroelectric behaviour. Also, in our analysis, to reduce experimental artefacts, we only focus on the modes with reasonable signal-to-noise ratio. Although only a limited number of phonon modes for each material is analysed (its $d\langle Q_j^2\rangle/dT$ partially contributes to $p_1^{(2)}$), our measured pyroelectric coefficients (Fig. 3h,i) for the similar thicknesses have the same trends with these phonon dynamic behaviours, especially for CBNO (about five times enhancement of pyroelectric coefficients between 40 nm and 250 nm versus about 2.8 times enhancement of $d\langle Q_j^2\rangle/dT$ of the in-plane phonon between 35 nm and 735 nm). The small enhancement for In_2Se_3 suggests that the contribution of the A_g^2 phonon to its pyroelectricity is small. It is possible that some phonons may have more pronounced contributions. However, their signal-to-noise ratios are too small to conduct reliable analysis. Nevertheless, these results evidence that the DW second-order effect associated with electron–phonon renormalization may play a possible role on the dimensionality effect for pyroelectricity.

Data availability

Source data for the main figures are provided with this paper. All data related to this study are available from the corresponding authors on request. Source data are provided with this paper.

41. Wang, B. & Gall, D. Fully strained epitaxial $Ti_{1-x}Mg_xN(001)$ layers. *Thin Solid Films* **688**, 137165 (2019).
42. Yuan, Y. et al. Three-dimensional atomic scale electron density reconstruction of octahedral tilt epitaxy in functional perovskites. *Nat. Commun.* **9**, 5220 (2018).
43. Vilaplana, R. et al. Experimental and theoretical studies on α-In_2Se_3 at high pressure. *Inorg. Chem.* **57**, 8241–8252 (2018).
44. Liu, L. et al. Atomically resolving polymorphs and crystal structures of In_2Se_3. *Chem. Mater.* **31**, 10143–10149 (2019).
45. Xu, C. et al. Two-dimensional ferroelasticity in van der Waals β′-In_2Se_3. *Nat. Commun.* **12**, 3665 (2021).
46. Klemenz Rivenbark, C. F. in *Springer Handbook of Crystal Growth* (eds Dhanaraj, G., Byrappa, K., Prasad, V. & Dudley, M.) 1041–1068 (Springer, 2010).
47. Morin, S. A., Forticaux, A., Bierman, M. J. & Jin, S. Screw dislocation-driven growth of two-dimensional nanoplates. *Nano Lett.* **11**, 4449–4455 (2011).
48. Lewis, B. The growth of crystals of low supersaturation: I. Theory. *J. Cryst. Growth* **21**, 29–39 (1974).
49. Guo, Y. et al. Unit-cell-thick domain in free-standing quasi-two-dimensional ferroelectric material. *Phys. Rev. Mater.* **5**, 044403 (2021).
50. Schilling, A. et al. Scaling of domain periodicity with thickness measured in $BaTiO_3$ single crystal lamellae and comparison with other ferroics. *Phys. Rev. B* **74**, 024115 (2006).
51. Taylor, D. Thermal expansion data. I: binary oxides with the sodium chloride and wurtzite structures, MO. *Trans. J. Br. Ceram. Soc.* **83**, 5–9 (1984).
52. Pathak, P. & Vasavada, N. Thermal expansion of NaCl, KCl and CsBr by X-ray diffraction and the law of corresponding states. *Acta Crystallogr. A* **26**, 655–658 (1970).
53. Jachalke, S. et al. The pyroelectric coefficient of free standing GaN grown by HVPE. *Appl. Phys. Lett.* **109**, 142906 (2016).
54. Lang, S. B. & Das-Gupta, D. K. in *Handbook of Advanced Electronic and Photonic Materials and Devices* (ed. Nalwa, H. S.) 1–55 (Academic Press, 2001).
55. Felix, P., Gamot, P., Lacheau, P. & Raverdy, Y. Pyroelectric, dielectric and thermal properties of TGS, DTGS and TGFB. *Ferroelectrics* **17**, 543–551 (1977).
56. Gebre, T., Batra, A. K., Guggilla, P., Aggarwal, M. D. & Lal, R. B. Pyroelectric properties of pure and doped lithium niobate crystals for infrared sensors. *Ferroelectr. Lett. Sect.* **31**, 131–139 (2004).
57. Beerman, H. P. Investigation of pyroelectric material characteristics for improved infrared detector performance. *Infrared Phys.* **15**, 225–231 (1975).
58. Tang, Y. et al. Composition, dc bias and temperature dependence of pyroelectric properties of ⟨111⟩-oriented $(1-x)Pb(Mg_{1/3}Nb_{2/3})O_3$–$xPbTiO_3$ crystals. *Mater. Sci. Eng. B* **119**, 71–74 (2005).
59. Sun, R. et al. Pyroelectric properties of Mn-doped $94.6Na_{0.5}Bi_{0.5}TiO_3$-$5.4BaTiO_3$ lead-free single crystals. *J. Appl. Phys.* **115**, 074101 (2014).
60. Liu, S. & Maciolek, R. Rare-earth-modified $Sr_{0.5}Ba_{0.5}Nb_2O_6$, ferroelectric crystals and their applications as infrared detectors. *J. Electron. Mater.* **4**, 91–100 (1975).

61. Mermin, N. D. Crystalline order in two dimensions. *Phys. Rev.* **176**, 250–254 (1968).
62. Yuzyuk, Y. I. Raman scattering spectra of ceramics, films, and superlattices of ferroelectric perovskites: a review. *Phys. Solid State* **54**, 1026–1059 (2012).
63. Jehng, J. M. & Wachs, I. E. Structural chemistry and Raman spectra of niobium oxides. *Chem. Mater.* **3**, 100–107 (1991).
64. Link, A. et al. Temperature dependence of the E_2 and A_1(LO) phonons in GaN and AlN. *J. Appl. Phys.* **86**, 6256–6260 (1999).
65. Balkanski, M., Wallis, R. F. & Haro, E. Anharmonic effects in light scattering due to optical phonons in silicon. *Phys. Rev. B* **28**, 1928–1934 (1983).
66. Sun, X., Shi, J., Washington, M. A. & Lu, T.-M. Probing the interface strain in a 3D-2D van der Waals heterostructure. *Appl. Phys. Lett.* **111**, 151603 (2017).
67. Postmus, C., Ferraro, J. R. & Mitra, S. S. Pressure dependence of infrared eigenfrequencies of KCl and KBr. *Phys. Rev.* **174**, 983–987 (1968).
68. Ager, J. W., Veirs, D. K. & Rosenblatt, G. M. Spatially resolved Raman studies of diamond films grown by chemical vapor deposition. *Phys. Rev. B* **43**, 6491–6499 (1991).

Acknowledgements This work is supported by the Air Force Office of Scientific Research under award number FA9550-18-1-0116, the US National Science Foundation under award numbers 1916652, 2031692 and 2024972, and the NYSTAR Focus Center at Rensselaer Polytechnic Institute under award number C180117. This paper is also supported by the U.S. National Science Foundation (Platform for the Accelerated Realization, Analysis, and Discovery of Interface Materials (PARADIM)) under Cooperative Agreement No. DMR-1539918 and made use of the Cornell Center for Materials Research (CCMR) Shared Facilities, which are supported through the NSF MRSEC Program (no. DMR-1719875). We thank J. Liu for the discussion on the mechanism of pyroelectricity. This research used resources of the Advanced Photon Source, a US Department of Energy (DOE) Office of Science user facility operated for the DOE Office of Science by Argonne National Laboratory under contract DE-AC02-06CH11357.

Author contributions J.S., J.J. and L.Z. conceived and developed the idea and planned the experiments. J.J. and L.Z. prepared the samples and devices and performed optical, scanning electron microscopy and AFM measurements. L.Z., J.J. and Y.H. performed the pyroelectric measurements. H.Z. performed synchrotron XRD measurements. P.B. and Y.S. performed MD simulations. Y.H. performed SHG measurements. J.J. performed Raman measurements. Y.G. and J.J. performed TEM and STEM measurements. B.W. and R.J. performed XRD measurements. Z.C., S.P. and X.W. contributed to the experimental set-ups and crystal growth. Y.X. performed AFM and RHEED measurements. Z.L. performed EBSD measurements. J.J. and L.Z. processed the data and J.J., L.Z. and J.S. interpreted the results. J.J. and L.Z. wrote the initial draft. J.S. revised the manuscript. C.M., Y.C., C.S., G.-C.W., T.-M.L., D.G., Y.-Y.S., N.K., E.F. and all the other authors were involved in the discussion for data analysis. J.S. supervised the project.

Competing interests The authors declare no competing interests.

Additional information

Supplementary information The online version contains supplementary material available at https://doi.org/10.1038/s41586-022-04850-7.

Correspondence and requests for materials should be addressed to Jie Jiang, Yunfeng Shi or Jian Shi.

Peer review information *Nature* thanks the anonymous reviewers for their contribution to the peer review of this work.